# applied optics

# General silicon-on-insulator higher-order mode converter based on substrip dielectric waveguides

Basma E. Abu-elmaaty,[1,2,*] Mohammed S. Sayed,[1] Ramesh K. Pokharel,[3] and Hossam M. H. Shalaby[1,4]

[1]*Department of Electronics and Communications Engineering, Egypt-Japan University of Science and Technology (E-JUST), Alexandria 21934, Egypt*
[2]*Electrical Engineering Department, Faculty of Engineering, Tanta University, Tanta, Egypt*
[3]*Graduate School of Information Science and Electrical Engineering, Kyushu University, Fukuoka 819-0395, Japan*
[4]*Electrical Engineering Department, Faculty of Engineering, Alexandria University, Alexandria 21544, Egypt*
*Corresponding author: basma.eldosouky@ejust.edu.eg*

A general silicon mode-converter waveguide that converts a fundamental mode to any higher-order mode is proposed. Specifically, dielectric substrip waveguides are inserted in the fundamental mode propagation path so that the conversion is done directly in the same propagation waveguide, without coupling the power into another waveguide as it happens in traditional mode converters. The device has a very small footprint compared to traditional converters. A mathematical model is developed to determine the design parameters of the used dielectric material and analyze the whole performance of the proposed device. Both the effective index method (EIM) and the perturbative mode-coupled theory are used in our mathematical analysis to get exact values for both the coupling coefficient and the length of the used dielectric material, so as to ensure a maximum coupled power transfer to the higher-order mode. In addition, full vectorial 3D-FDTD simulations are performed to validate our mathematical model. Our results show good agreement between the approximate EIM method and accurate full vectorial 3D-finite-difference time-domain (FDTD) simulations in characterizing the device parameters and performance. In order to validate the design model, two mode converters are simulated, fabricated, and tested for converting a fundamental $TE_0$ mode into both first- and second-order ($TE_1$ and $TE_2$) modes, respectively. Good insertion losses and low crosstalks are obtained. Good agreement between simulated and fabricated results are achieved.     © 2019 Optical Society of America

https://doi.org/10.1364/AO.58.001763

## 1. INTRODUCTION

Along with the rapid development of photonics integrated systems, on-chip mode converters are serving as important components in multiplexing techniques [1–5]. Currently, mode-division multiplexing (MDM) and simultaneous mode- and polarization-division-multiplexing techniques are getting much interest as they provide high on-chip data transmission rates [6–11]. Indeed, the transmission capacity of on-chip optic systems can be increased by increasing the number of allowed modes in MDM systems [12]. Normally these techniques require mode conversions from fundamental modes to higher-order modes before multiplexing on a multimode waveguide [12].

One of the most commonly used methods for mode conversion in optical fiber communication systems is based on the use of phase plates, due to its simplicity and good selectivity

conversion at the design wavelength [13–15]. To selectively excite one specific mode, it is enough to match the phase profile of that particular mode, which can be achieved through phase modulation of the input field by placing a proper phase element in its path [16]. Tilted binary phase plates have been investigated in optical communications systems for dynamic and efficient mode conversion not only for the design wavelength but also over a wide spectral range [17]. Phase plates, which phase patterns match that of higher-order modes, are made of glass with thicker part of its surface. This introduces a phase jump of $\pi$ to the light that passes through it [13]. This phase plate has many phase patterns for different higher-order modes [13].

Due to the increasing use of silicon-on-insulator (SOI) in the manufacture of integrated circuits because of its advantages in high speed and low power requirements [18], the mode conversion process in SOI is getting great attention as being a basic part of on-chip platforms. The traditional techniques

adopted for on-chip mode converters are based on traditional directional couplers and Bragg grating couplers [19,20]. In traditional coupling methods, an optical field is converted from one mode to another by precisely designing the coupling gap, the coupling length, as well as determining the grating parameters. These coupling techniques depend on coupling the optical power from its main propagation path to another waveguide and their coupling lengths cannot be very short [21]. These methods face great difficulty in setting precise values of their design parameters due to device parameter variations from fabrication [22].

Another strategy has been investigated by etching different shapes in the propagation waveguide to produce a perturbation in the refractive index distribution, and accordingly some of the electromagnetic energy propagating in one mode would couple into another mode [23–25]. For the conversion from fundamental ($TE_0$) to first-order ($TE_1$) mode, a dielectric metasurface consisting of nanoscale features etched into a 1 μm × 220 nm waveguide has been proposed in [24]. The mode converter has an 88% transmission and is 23 μm long. A $TE_0$ to $TE_1$ mode converter with a small footprint of 0.8 μm × 5.3 μm and 0.95 transmittance has been realized by two cascaded trenches fully etched inside a silicon nanowire [25].

Also, a $TE_0/TE_1$ mode conversion Bragg grating device incorporating resonant cavity section has been reported to obtain narrow transmission wavelength peak [26]. The device has a large footprint where its length is greater than 127 μm using single resonance cavity structure, and can be double this length using a double cavity structure. In addition, a topology optimization method has also been used for fundamental to first-order mode conversion [27]. The device has a cross-sectional area of 1.4 μm × 3.4 μm, and achieves an insertion loss (IL) less than 2 dB and extinction ratio greater than 9.5 dB. In addition, this topology optimization has been employed to design a device that allows for reversible conversion between the fundamental $TE_0$ mode and second-order $TE_2$ mode [27].

In [28], we have proposed a broadband silicon-silicon nitride (Si – $Si_3N_4$) dual polarized mode converter for SOI technology. The device converts a fundamental $TE_0$ ($TM_0$) mode in a silicon multimode waveguide into a first-order $TE_1$ ($TM_1$) mode over a wide spectrum range. The device has a very small footprint, as it is composed of an etched silicon nitride substrip of length 0.8 μm on half-width of a 1 μm × 220 nm silicon strip waveguide for TE polarization. The device characteristics have been evaluated using simulation without fabrication verification.

In this paper, we extend the idea in [28] to higher-order modes. In addition, we fabricate the device to validate the simulation results. Specifically, the fundamental mode in its propagation path is divided into a number of equal parts depending on the mode number of the desired higher-order mode. Phase shifts are introduced to some of these parts by forcing them to propagate through substrips of different dielectric materials, each of length $d$. That is, the substrips are used to readjust the relative phase differences among the fundamental mode parts and excite the desirable higher-order mode. In particular, we focus on the design of $TE_0$ to $TE_1/TE_2$ mode

converters and evaluate their performances through simulation and fabrication.

We start by developing a mathematical model for a fundamental to first-order mode converter using both the effective-index method (EIM) [29–33] and coupled-mode theory [34]. This mathematical model helps in determining both the coupling coefficients and system design parameters. Next, full vectorial 3D-FDTD simulations are performed for both the first- and second-order mode converters to verify the developed mathematical model. The two mode converters are designed and simulated using two different dielectric materials: silicon nitride $Si_3N_4$ and silicon dioxide $SiO_2$. Finally, the devices are fabricated and tested to validate the proposed model using only $SiO_2$ material. The results show that the insertion loss ranges from 1.28 dB to 1.9 dB for different modes using different dielectric materials with a length of only 0.6–0.8 μm.

The remaining of this paper is organized as follows. The device structures of both first- and second-order mode converters are presented in Section 2. It includes a general equation to determine the number and positions of dielectric substrips that divide the fundamental mode. Section 3 is devoted for the mathematical model development and educing formulas for both the coupling coefficient and system design parameters. 3D-FDTD simulations based on our theoretical results are presented in Section 4. The fabrication process is described in Section 5. The experimental data and the measurement results are analyzed, in the same section, to get the insertion losses and crosstalk (CT) for converted higher-order modes. Finally, our conclusions are given in Section 6.

## 2. DEVICE STRUCTURE AND MODE PROFILE

The $m$th-order mode converter, $m \in \{1, 2, \ldots\}$, consists of one multimode waveguide of width $w$, notched with a number of small parts of dielectric material (substrips), each of length $d$ and width $w/(m+1)$. These substrips provide phase jumps of $\pi$ relative to that of light propagating through the silicon part. That is, they create a phase pattern like that of the desired higher-order mode. For example, the first-order mode converter, which converts the fundamental $TE_0$ mode to first-order $TE_1$ mode, is formed using one substrip of length $d$ and width $w/2$, as shown in Fig. 1(a). Also, the second-order mode converter is formed using two substrips, each of length $d$
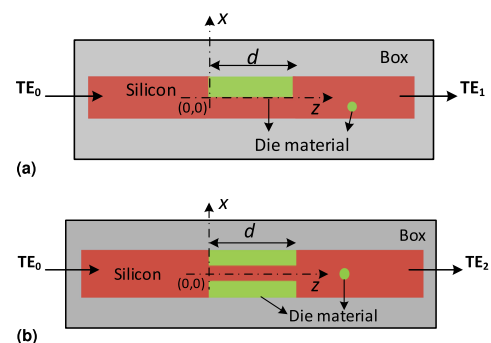


**Fig. 1.** Structure of proposed (a) $TE_0$ to $TE_1$ and (b) $TE_0$ to $TE_2$ waveguide mode converters.

and width $w/3$, as shown in Fig. 1(b). In addition, a notched circle, of the same dielectric material as that of the substrips, with radius $R$ is placed after the phase pattern in order to enhance the coupled power to the higher-order mode and reduce the crosstalk to the fundamental mode. The proposed mode conversion process is based on the phase retardation technique. This technique has been adopted in optical fibers, but it is the first time to be implemented on SOI platforms directly in the same propagation waveguide.

### A. Spatial Distributions of Substrips

The dielectric substrips would readjust the relative phase differences among divided $(m + 1)$ parts and excite the desired higher-order mode. The number of dielectric substrips and their spatial distributions can be determined based on the phase distribution of the higher-order mode by a transmittance function of the $(N - 1)$th-order mode $T_{N-1}(x, z)$, $N = m + 1$. The transmittance functions for both odd and even higher-order modes are given by Eq. (1):

$$T_{N-1}(x,z) = \begin{cases} 1; & \text{if } x \in \left\{\bigcup_{n=0}^{(N-2)/4}\left(2n\frac{w}{N}, (2n+1)\frac{w}{N}\right]\right\} \cup \left\{\bigcup_{n=1}^{N/4}\left[-2n\frac{w}{N}, -(2n-1)\frac{w}{N}\right)\right\} \\ -1; & \text{if } x \in \left\{\bigcup_{n=0}^{(N-2)/4}\left[-(2n+1)\frac{w}{N}, -2n\frac{w}{N}\right)\right\} \cup \left\{\bigcup_{n=1}^{N/4}\left((2n-1)\frac{w}{N}, 2n\frac{w}{N}\right]\right\} \end{cases} ; \quad \text{for odd – order modes,}$$

$$T_{N-1}(x,z) = \begin{cases} 1; & \text{if } |x| \in \bigcup_{n=0}^{(N-1)/4}\left(\frac{w}{2N} + (2n-1)\frac{w}{N}, \frac{w}{2N} + 2n\frac{w}{N}\right] \\ -1; & \text{if } |x| \in \bigcup_{n=1}^{(N-3)/4}\left(\frac{w}{2N} + 2n\frac{w}{N}, \frac{w}{2N} + (2n+1)\frac{w}{N}\right] \end{cases} ; \quad \text{for even – order modes.}$$

(1)

### B. Perturbation of the Refractive Index

In our mathematical development, we aim at determining the design parameters for the first-order mode converter. Although our focus is for first-order mode converters, the mathematical model can be easily extended to higher-order mode converters.

According to Eq. (1), the first-order mode converter consists of one dielectric substrip of width $w/2$ and length $d$. By ditching this substrip in the propagation waveguide, a perturbation in the refractive index distribution is created and some of the electromagnetic energy propagating in the fundamental mode would couple into the first-order mode. The perturbation of the refractive index distribution $\Delta n^2(x, y)$ is obtained by subtracting the refractive index of the perturbed system from that of the unperturbed system [Fig. 1(a)]:

$$\Delta n^2(x,y) = \begin{cases} n_{\text{Die}}^2 - n_{\text{Si}}^2; & \text{if } 0 \le z \le d, 0 \le x \le w/2, \\ 0; & \text{otherwise,} \end{cases}$$

$$= (n_{\text{Die}}^2 - n_{\text{Si}}^2) \cdot \text{rect}\left(\frac{z - \frac{d}{2}}{d}\right) \cdot \text{rect}\left(\frac{x - \frac{w}{4}}{\frac{w}{2}}\right), \quad \text{(2)}$$

where $n_{\text{Si}}$ and $n_{\text{Die}}$ are the refractive indices of silicon and the dielectric substrip material, respectively.

### C. Mode Profiles

Using EIM, we can find the 2D mode profile of our first-order strip waveguide mode converter. That is, the profile can be written as $\Psi_m(x, y) = G(y)F(x)$, where $G(y)$ and $F(x)$ are the electric fields of two slab waveguides in the $y$- and $x$-directions, respectively [32]. The electric field in the $y$-direction is

$$G(y) = \begin{cases} A \cos(\rho h/2)e^{\gamma(y+h/2)}; & \text{if } y < -h/2, \\ A \cos(\rho y); & \text{if } |y| \le h/2, \\ A \cos(\rho h/2)e^{-\gamma(y-h/2)}; & \text{if } y > h/2, \end{cases} \quad \text{(3)}$$

where $A$ is a constant. The parameters $\rho$ and $\gamma$ are given by

$$\rho = \frac{2\pi}{\lambda_0}\sqrt{n_{\text{Si}}^2 - n_{\text{eff}_g}^2},$$

$$\gamma = \frac{2\pi}{\lambda_0}\sqrt{n_{\text{eff}_g}^2 - n_c^2}, \quad \text{(4)}$$

respectively. Here, $n_{\text{eff}_g}$ is the effective index of a slab waveguide of height $h$ in the $y$-direction, $n_c$ is the refractive index of the clad, and $\lambda_0$ is the operating wavelength. In the $x$-direction, the electric field $F_m(x)$ of the $m$th-order mode, $m \in \{0, 1, 2, \ldots\}$, of the propagating waveguide is

$$F_m(x) = \begin{cases} \frac{N_{\text{wg}_m}\eta_0}{n_c^2}C_m\cos(\alpha_m w/2 + m\pi/2) \\ \quad \cdot e^{\sigma_m(x+w/2)}; & \text{if } x < -w/2, \\ \frac{N_{\text{wg}_m}\eta_0}{n_{\text{eff}_g}^2}C_m\cos(\alpha_m x - m\pi/2); & \text{if } |x| \le w/2, \\ \frac{N_{\text{wg}_m}\eta_0}{n_c^2}C_m\cos(\alpha_m w/2 - m\pi/2) \\ \quad \cdot e^{-\sigma_m(x-w/2)}; & \text{if } x > w/2, \end{cases} \quad \text{(5)}$$

where $C_m$ is a constant, $N_{\text{wg}_m}$ is the final effective index of the waveguide, and $\eta_0 = \sqrt{\mu_0/\epsilon_0}$ is wave impedance in free space, where $\mu_0$ and $\epsilon_0$ are free space permeability and permittivity, respectively. In addition, $\alpha_m$ and $\sigma_m$ are given by

$$\alpha_m = \frac{2\pi}{\lambda_0}\sqrt{n_{\text{eff}_g}^2 - N_{\text{wg}_m}^2}, \qquad \sigma_m = \frac{2\pi}{\lambda_0}\sqrt{N_{\text{wg}_m}^2 - n_c^2}, \quad \text{(6)}$$

respectively.

The constants $A$ and $C_m$ are chosen so that power flow in the $z$-direction is unity. Using Eqs. (3) and (5), we can extract the orthogonality property for strip waveguides:

$$\iint \Psi_n^*(x,y)\Psi_m(x,y)dxdy = \frac{2\eta_0^2 N_{\text{wg}n}}{n_{\text{eff}_g}^3}\delta_{nm}, \qquad \textbf{(7)}$$

where $\delta_{nm}$ is the Kronecker delta.

## 3. COUPLED-MODE EQUATIONS

In this section, we aim at finding a system of first-order coupled differential equations that relates the amplitudes of the forward propagating modes for the waveguide using coupled-mode theory. The electric field in the propagating waveguide can be expressed as

$$E(x,y,z) = \sum_m \mathcal{A}_m(z)\Psi_m(x,y)e^{-j\beta_m z}, \qquad \textbf{(8)}$$

where $\mathcal{A}_m(z)$ is the complex amplitude of the $m$th-order mode in the propagation waveguide. In addition, $\Psi_m(x,y)$ is the electric field profile for the $m$th-order mode and

$$\frac{d\mathcal{A}_n}{dz}e^{-j\beta_n z} = -j\sum_m \kappa_{nm}\mathcal{A}_m(z)e^{-j\beta_m z}, \qquad \textbf{(11)}$$

where the coupling coefficient is

$$\kappa_{nm} = \frac{\omega\epsilon_0 n_{\text{eff}_g}^3}{4\eta_0 N_{\text{wg}_n}^2}\iint_{\substack{|y|\le h/2 \\ 0\le x\le w/2}} \Psi_n^*(x,y)(n_{\text{Die}}^2 - n_{\text{Si}}^2)\Psi_m(x,y)dxdy. \qquad \textbf{(12)}$$

Performing the double integration, the coupling coefficient is given by Eq. (13). The coupling coefficient $\kappa_{nm}$ is an important parameter to the device performance as it controls the coupling between the input mode $n$ and output mode $m$ through the propagation waveguide in the forward direction:

$$\kappa_{nm} = \frac{\omega\epsilon_0 n_{\text{eff}_g}^3}{4\eta_0 N_{\text{wg}_n}^2} \times (n_{\text{Die}}^2 - n_{\text{Si}}^2)\left(\frac{h}{2} + \frac{\gamma}{\gamma^2 + \rho^2}\right)A^2 \times \frac{N_{\text{wg}_n}\eta_0}{n_{\text{eff}_g}^2}C_n \times \frac{N_{\text{wg}_m}\eta_0}{n_{\text{eff}_g}^2}C_m$$
$$\times \left\{\frac{\left(\frac{n_{\text{eff}_g}}{n_c}\right)^2(\sigma_n - \sigma_m)}{(\alpha_n^2 - \alpha_m^2)\sqrt{1 + \left[\left(\frac{n_{\text{eff}_g}}{n_c}\right)^2\frac{\sigma_n}{\alpha_n}\right]^2}\sqrt{1 + \left[\left(\frac{n_{\text{eff}_g}}{n_c}\right)^2\frac{\sigma_m}{\alpha_m}\right]^2}} + \frac{\alpha_n\sin\left(n\frac{\pi}{2}\right)\cos\left(m\frac{\pi}{2}\right) - \alpha_m\sin\left(m\frac{\pi}{2}\right)\cos\left(n\frac{\pi}{2}\right)}{\alpha_n^2 - \alpha_m^2}\right\}. \qquad \textbf{(13)}$$

$\beta_m = 2\pi N_{\text{wg}_m}/\lambda_0$ is its propagation constant. Here, $N_{\text{wg}_m}$ denotes the effective index of the $m$th-order mode. Starting from the wave equation for perturbed and unperturbed systems, and following the procedure in [34,35], we obtain

$$j2\sum_m \beta_m\Psi_m(x,y)\frac{d\mathcal{A}_m}{dz}e^{-j\beta_m z}$$
$$= k_0^2\Delta n^2(x,y,z)\cdot\sum_m\mathcal{A}_m(z)\Psi_m(x,y)e^{-j\beta_m z}. \qquad \textbf{(9)}$$

Multiplying the last equation by $\Psi_n^*(x,y)$, integrating over both $x$ and $y$, and using orthogonality property Eq. (7), we get

$$j2\beta_n\frac{2\eta_0^2 N_{\text{wg}_n}}{n_{\text{eff}_g}^3}\frac{d\mathcal{A}_n}{dz}e^{-j\beta_n z}$$
$$= k_0^2\sum_m\mathcal{A}_m(z)\cdot\text{rect}\left(\frac{z - \frac{d}{2}}{d}\right)e^{-j\beta_m z}$$
$$\iint_{\substack{|y|\le h/2 \\ 0\le x\le w/2}} \Psi_n^*(x,y)(n_{\text{Die}}^2 - n_{\text{Si}}^2)\Psi_m(x,y)dxdy, \qquad \textbf{(10)}$$

where $\Delta n^2(x,y,z)$ is substituted from Eq. (2). Focusing our attention within length $0 \le z \le d$ of the phase plate, where outside this region there is no coupling between any modes:

We assume that the propagation waveguide in our mode converter supports only three modes $\{0, 1, 2\}$ with only one input mode $n$, an output (converted) mode $m$, and an interfering mode $i$. Applying this constraint to Eq. (11), we get the following coupled-mode equations:

$$\frac{d\mathcal{A}_n}{dz}e^{-j\beta_n z} = -j\kappa_{nn}\mathcal{A}_n(z)e^{-j\beta_n z} - j\kappa_{nm}\mathcal{A}_m(z)e^{-j\beta_m z}$$
$$- j\kappa_{ni}\mathcal{A}_i(z)e^{-j\beta_i z},$$
$$\frac{d\mathcal{A}_m}{dz}e^{-j\beta_m z} = -j\kappa_{mm}\mathcal{A}_m(z)e^{-j\beta_m z} - j\kappa_{mn}\mathcal{A}_n(z)e^{-j\beta_n z}$$
$$- j\kappa_{mi}\mathcal{A}_i(z)e^{-j\beta_i z},$$
$$\frac{d\mathcal{A}_i}{dz}e^{-j\beta_i z} = -j\kappa_{ii}\mathcal{A}_i(z)e^{-j\beta_i z} - j\kappa_{im}\mathcal{A}_m(z)e^{-j\beta_m z}$$
$$- j\kappa_{in}\mathcal{A}_n(z)e^{-j\beta_n z}. \qquad \textbf{(14)}$$

Defining

$$\chi_n = \mathcal{A}_n e^{-j\beta_n z}, \quad \chi_m = \mathcal{A}_m e^{-j\beta_m z}, \quad \chi_i = \mathcal{A}_i e^{-j\beta_i z}, \qquad \textbf{(15)}$$

Eq. (14) reduces to

$$\frac{d\chi_n}{dz} = -j(\beta_n + \kappa_{nn})\chi_n - j\kappa_{nm}\chi_m - j\kappa_{ni}\chi_i,$$

$$\frac{d\chi_m}{dz} = -j\kappa_{mn}\chi_n - j(\beta_m + \kappa_{mm})\chi_m - j\kappa_{mi}\chi_i,$$

$$\frac{d\chi_i}{dz} = -j\kappa_{in}\chi_n - j\kappa_{im}\chi_m - j(\beta_i + \kappa_{ii})\chi_i. \quad \text{(16)}$$

The last set of equations can be written in matrix form:

$$\frac{d\boldsymbol{X}}{dz} = \boldsymbol{AX}, \quad \text{(17)}$$

where

$$\boldsymbol{X} = \begin{bmatrix} \chi_n \\ \chi_m \\ \chi_i \end{bmatrix} \quad \text{(18)}$$

and

$$\boldsymbol{A} = \begin{bmatrix} -j(\beta_n + \kappa_{nn}) & -j\kappa_{nm} & -j\kappa_{ni} \\ -j\kappa_{mn} & -j(\beta_m + \kappa_{mm}) & -j\kappa_{mi} \\ -j\kappa_{in} & -j\kappa_{im} & -j(\beta_i + \kappa_{ii}) \end{bmatrix}. \quad \text{(19)}$$

Knowing the initial values at the input $z = 0$,

$$\boldsymbol{X}(0) = \begin{bmatrix} \chi_n(0) \\ \chi_m(0) \\ \chi_i(0) \end{bmatrix} = \begin{bmatrix} \mathcal{A}_n(0) \\ 0 \\ 0 \end{bmatrix}, \quad \text{(20)}$$

we get the solution of Eq. (17) as

$$\boldsymbol{X}(z) = e^{\boldsymbol{A}z}\boldsymbol{X}(0). \quad \text{(21)}$$

From the last general solution, we can evaluate the optimum length of the phase plate which ensures that maximum power is coupled from the input mode $n$ to output mode $m$.

Although, the previous mathematical model is performed for first-order mode converters, it can be extended easily to higher-order mode converters. This depends only on the order of the mode, and corresponding number and spatial distributions of dielectric substrips as indicated in Eq. (1).

## 4. 3D-FDTD SIMULATION AND NUMERICAL RESULTS

In this section, we perform 3D-FDTD simulations on both first- and second-order mode converters and present the simulation results. In our simulation, we use a strip waveguide with SiO$_2$ cladding and buried oxide of 2 μm. The design parameters of the mode converters are determined using the theoretical expressions developed in the previous section. The designs and simulations are performed for two different substrip materials: silicon nitride (Si$_3$N$_4$) with refractive index $n_{Si_3N_4} = 2.016$ and silicon dioxide (SiO$_2$) with refractive index $n_{SiO_2} = 1.44$.

### A. First-Order Mode Converter

In the case of the TE$_0$/TE$_1$ waveguide mode converter, a 1 μm × 220 nm strip waveguide is used.

#### 1. Design Parameters Evaluation

The first-order mode converter is composed of one dielectric substrip with width $w/2$ and length $d$ as demonstrated in Eq. (1) for $m = 1$. Using the solution of the coupled-mode
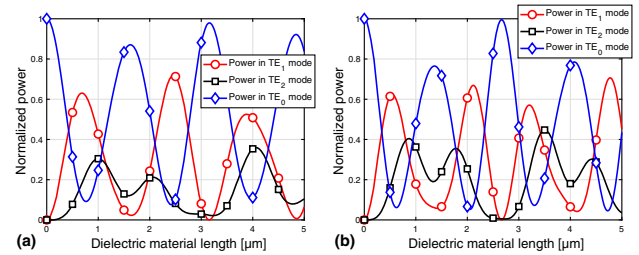


**Fig. 2.** Normalized power in all the supported modes in the TE$_0$/TE$_1$ mode converter for (a) Si$_3$N$_4$, (b) SiO$_2$ substrip material.

equations Eq. (21), we determine the smallest length $d$ of the dielectric material to guarantee maximum power transfer to the first-order mode.

Figure 2 shows the normalized power for all three supported modes versus the substrip length. It is clear from the figure that the smallest lengths for maximum power transfer are achieved at $d \cong 0.68$ μm and $d \cong 0.55$ μm for silicon nitride, Fig. 2(a), and silicon dioxide, Fig. 2(b), respectively. It is also noticed from Fig. 2 that the conversion to the first-order mode is achieved at different lengths of the dielectric substrip which correspond to maximum power transfer (the peaks of the power curves). High crosstalks to the second-order modes are noticed, i.e., some power is transferred from the fundamental mode to the TE$_1$ mode. This motivates us to add a notched circle of the same substrip material. The dimension and position of the circle are optimized to achieve maximum power coupling to the TE$_1$ mode as well as minimum power coupling to other modes.

#### 2. 3D-FDTD Simulation of First-Order Mode Converter

In this subsection, we use 3D-FDTD Solutions to simulate the performance of the proposed first-order mode converter in a 220 nm height strip waveguide with SiO$_2$ cladding and BOX of 2 μm. In our simulation, we use the obtained parameters as determined in the last subsection. The performance is determined in terms of both the IL and CT, defined in decibels as

$$\text{IL} = 10 \log_{10} \frac{P_m(L)}{P_n(0)}, \quad \text{CT} = 10 \log_{10} \frac{P_i(L)}{P_n(0)}, \quad \text{(22)}$$

where $P_m$ is the power of the $m$th mode and $L$ is the device length. For the first-order mode converter, we have $n = 0$, $m = 1$, and $i \in \{0, 2\}$.

The simulation results when using Si$_3$N$_4$ material have been illustrated in [28]. Figure 3(a) shows the transmission results
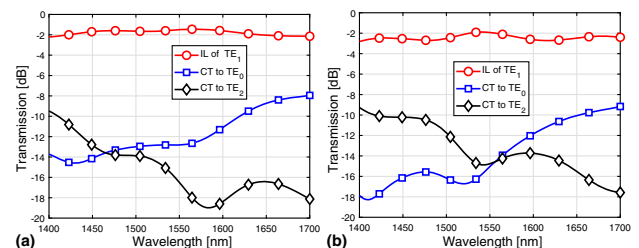


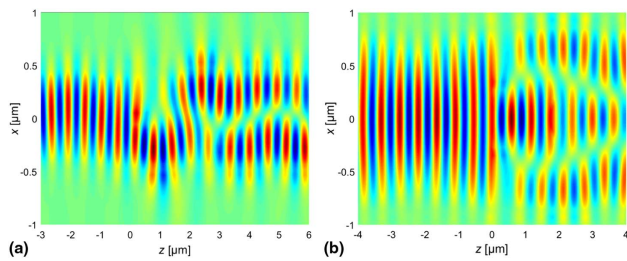**Fig. 3.** Insertion loss and crosstalks for TE$_0$ to TE$_1$ mode converter using (a) Si$_3$N$_4$ material, (b) SiO$_2$ material.

**Fig. 4.** 3D-FDTD electric field propagation for (a) $TE_0$ to $TE_1$ mode converter, (b) $TE_0$ to $TE_2$ mode converter.



**Fig. 5.** Insertion loss and crosstalks for $TE_0$ to $TE_2$ mode converter using (a) $Si_3N_4$ material, (b) $SiO_2$ material.

for the sake of comparison. At an operating wavelength of 1550 nm, we can observe that the conversion into the $TE_1$ mode is achieved with an insertion loss of –1.5 dB and crosstalks of –12.8 dB and –16.73 dB to both fundamental $TE_0$ and second-order $TE_2$ modes, respectively.

In addition, the device is designed when using $SiO_2$ material with length $d = 0.6$ μm (as obtained from FDTD sweeping) and with a circle of radius 70 nm placed at position $(z, x) = (2.6, -0.3)$ μm. The diameter and position of the circle are optimized to achieve maximum power transfer to the $TE_1$ mode and minimum power coupling to other modes. The 3D-FDTD simulation results in this case are illustrated in Fig. 3(b). It is clear from the figure that the conversion into the $TE_1$ mode is achieved at 1550 nm with an insertion loss of –1.9 dB and crosstalks of –15.13 dB and –14.79 dB to both fundamental $TE_0$ and second-order $TE_2$ modes, respectively.

It is clear from Fig. 3 that the silicon nitride material provides a better insertion loss for the $TE_1$ mode, but the $SiO_2$ mode converter has a lower crosstalk to the fundamental $TE_0$ mode.

The 3D-FDTD field propagation of our mode converter is illustrated in Fig. 4(a) when exciting the device by a $TE_0$ mode at the input of the waveguide. Conversion to the $TE_1$ mode is clear after passing through the dielectric substrip.

## B. Second-Order Mode Converter

A $TE_0/TE_2$ mode converter is designed following similar steps as illustrated in the last subsection and simulated for a 1.8 μm × 220 nm strip waveguide. Unlike the first-order mode, the second-order mode is an even mode which has a phase distribution determined from Eq. (1) with $m = 2$. Accordingly, we need two substrips of the dielectric material, each with a length $d$ and a width $w/3$ to equally divide the fundamental mode into three parts. Two parts propagate in the two dielectric substrips and encounter phase shifts of $\pi$ relative to the other part which propagates in the silicon material. Finally, the light is accumulated in the second-order mode.

Starting from Eq. (10) (with integration split into two parts for two dielectric substrips) and following a similar procedure, we can extract the length $d$ that ensures maximum power transfer to the second-order mode.

### 1. 3D-FDTD Simulation of Second-Order Mode Converter

3D-FDTD simulations are performed to evaluate the performance of the proposed second-order mode converter for both
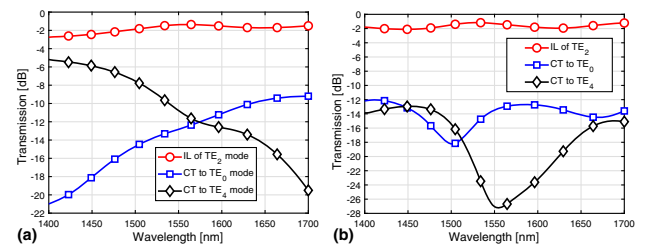
silicon nitride and silicon dioxide materials, and the simulated results are plotted in Figs. 5(a) and 5(b), respectively. Here both the IL and CT are defined as in Eq. (22) with $n = 0, m = 2$, and $i \in \{0, 1, 3, 4\}$.

For the mode converter with $Si_3N_4$ material, the length $d = 0.6$ μm and the notched circle has a radius 175 nm and is placed at position $(z, x) = (1.9, 0)$ μm. For the mode converter with $SiO_2$, we use same waveguide parameters, except that the circle radius is reduced to 140 nm and placed at position $(z, x) = (2.2, 0)$ μm. From Fig. 5(a), we can clearly observe that at 1550 nm, the conversion into the $TE_2$ mode occurs with an insertion loss of –1.4 dB and crosstalks of –12.8 dB and –11 dB to both fundamental $TE_0$ and $TE_4$ modes, respectively. On the other hand, Fig. 5(b) shows that the conversion into the $TE_2$ mode is accomplished at 1550 nm with an insertion loss of –1.28 dB and crosstalks of –13.5 dB and –26.96 dB to both fundamental $TE_0$ and $TE_4$ modes, respectively. A comparison between the last two mode converters indicates that the one which uses $SiO_2$ has a better performance.

The field propagation of this converter is illustrated in Fig. 4(b). Conversion to the $TE_2$ mode is clear after passing through the dielectric substrips.

## C. Effect of the Notched Circle

In this subsection, we discuss the effect of the notched circle on the performance of mode converters. The notched circle is placed in the light propagation path after the mode conversion occurs using dielectric substrips. The mode conversion using only phase retardation has high crosstalks to the unwanted modes, as shown in Fig. 2. We reduce this crosstalk by inserting a notched circle with optimized dimension and position. This circle produces a perturbation to the refractive index which makes a fluctuation in the power propagation in the supported modes. This added perturbation is optimized to diminish the power loss that exists in the undesirable modes.

In Fig. 6, we plot the transmission through the $TE_0/TE_1$ silicon nitride mode converter with and without the use of the notched circle. It is clear that the conversion into the $TE_1$ mode without the perturbation circle is achieved at 1550 nm with an insertion loss of –2.2 dB and crosstalks of –10.87 dB and –9.77 dB to both $TE_0$ and $TE_2$ modes, respectively. After inserting the circle, the coupled power to the $TE_1$ mode increases and the IL improves to –1.5 dB, and the crosstalks to the $TE_0$ and $TE_2$ modes improve to –12.8 dB and –16.78 dB, respectively. In fact, the circle makes small disturbance in the
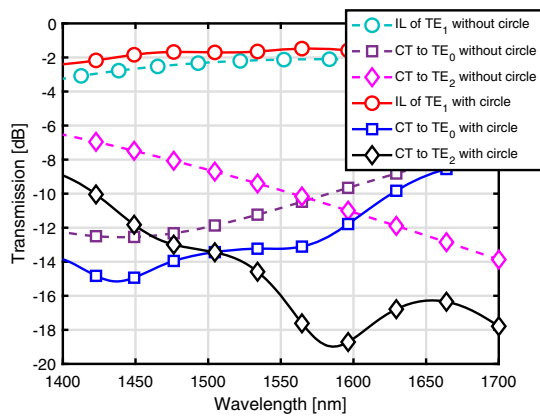
**Fig. 6.** Insertion loss and crosstalks for $TE_0$ to $TE_1$ mode converter using $Si_3N_4$ material with and without a notched circle.



**Fig. 7.** Schematic of the whole device with different components for (a) $TE_0$ to $TE_1$ mode converter, (b) $TE_0$ to $TE_2$ mode converter.



**Fig. 8.** SEM images with different components of fabricated systems for both $TE_0/TE_1$ and $TE_0/TE_2$ mode converters.

propagating modes as it divides the power in the mode into two parts, so the position and size of this circle is crucial.

## 5. EXPERIMENTAL RESULTS

Our devices have been fabricated (for both $TE_0/TE_1$ and $TE_0/TE_2$ mode converters) using 100 keV *electron beam lithography*. A silicon-on-insulator wafer of 200 mm diameter, 220 nm device thickness, and 2 μm buffer oxide thickness has been used as the base material for the fabrication. A 2.2 μm oxide cladding has been deposited using a plasma-enhanced chemical vapor deposition process based on tetraethyl orthosilicate at 300°C. The devices have been inspected using a scanning electron microscope (SEM) to verify patterning and etch quality. Reflectometry measurements have been performed throughout the process to verify the device layer, buffer oxide, and cladding thicknesses before delivery. Spectrum analysis has been measured using a spectrum laser source, which can be swept over 1500 nm. A polarization-maintaining single-mode fiber array has been used to couple light in/out of the chip. The fiber array has a channel pitch of 127 μm and all on-chip grating couplers are spaced with the same distance so as to allow automated measurements for devices.

### A. Circuit Description for Both $TE_0/TE_1$ and $TE_0/TE_2$ Mode Converters

Figures 7(a) and 7(b) show schematic diagrams of the whole circuits with different parts that have been used in the fabrication of both first- and second-order mode converters, respectively. The SEM images of the fabricated devices are illustrated in Fig. 8. The fabricated structures for the $TE_0/TE_1$ mode converter are located at both the right and left of Fig. 8(b), whereas that for the $TE_0/TE_2$ mode converter are located at the center of both Figs. 8(a) and 8(b).

The proposed devices have been fabricated using silicon dioxide material as an etched dielectric material. Grating couplers have been used to couple light from the fiber to the fundamental mode on an input waveguide of width 500 nm. The waveguides used in the proposed mode converter have different widths, so they are connected to the I/O ports by tapers to reduce backreflections and maintain the power in the desired
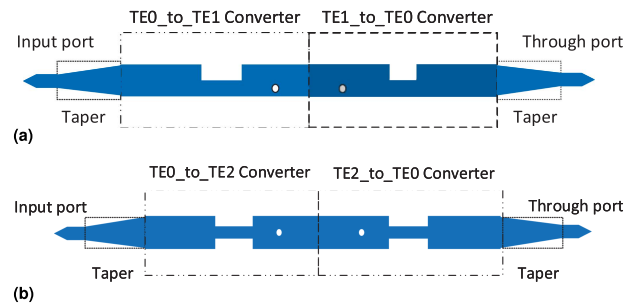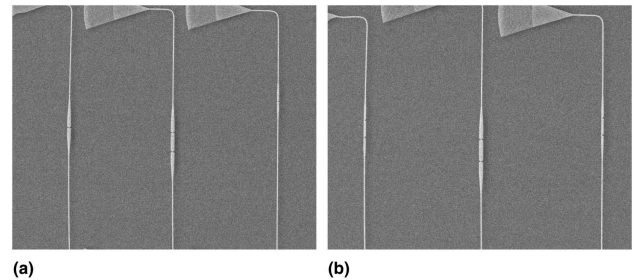
mode. A taper and its inverse are used to allow the detection of the fundamental mode in the 1 μm and 1.8 μm waveguides via grating couplers in the first- and second-order mode converters, respectively, as shown in Figs. 7(a) and 7(b). The proposed mode converter is a reciprocal device, i.e., it converts $TE_0/TE_1$ ($TE_0/TE_2$) and $TE_1/TE_0$ ($TE_2/TE_0$) with same insertion losses. Accordingly, an inverse mode converter has been used to restore the power to the fundamental mode so as to be coupled out through an output grating coupler.

An indirect calibration method has been used to extract the IL of our higher-order mode converter, which depends on reference circuit(s) to eliminate the loss due to irrelevant components. One reference circuit is a grating coupler pair with a single-mode waveguide between them, from which we can get the IL of the grating coupler alone. Next, we design a circuit that is composed of a grating coupler pair, the proposed mode converter, and its inverse converter, as shown in Fig. 7. Accordingly, we can determine the performance of our mode converter by subtracting the IL of the grating coupler alone from the IL of the whole fabricated circuit and then dividing the obtained IL by two.

### 1. Grating Coupler Pair Layout

The grating coupler has a finite bandwidth which affects the measured data of our device. To correct this, the base line shape of the grating coupler must be removed. One method of removing this shape is by fitting its measured data to a low-order polynomial and then truncating our analysis to the top 10 dB of the grating coupler response to avoid noise introduced at the end of the spectrum. The grating coupler pair layout and its
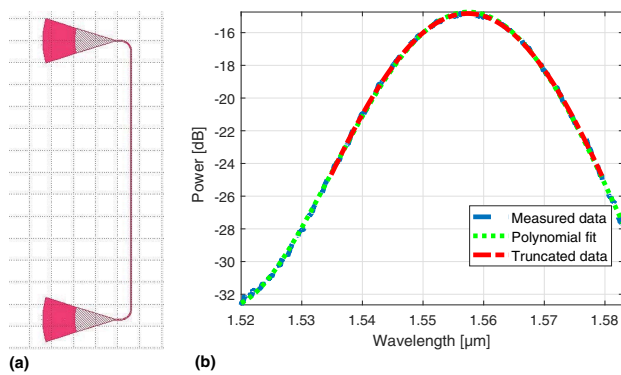
**Fig. 9.**   (a) Grating coupler pair layout. (b) Measured, fitted, and truncated data.

fabricated data are shown in Fig. 9. The two fiber grating couplers are designed at 1550 nm quasi-TE operation.

### B. Experimental Data

A fundamental mode is provided to test our devices through a TE-polarized grating coupler. In the first-order mode converter, a taper of length 6 μm is used to couple the fundamental mode from a 500 nm single-mode waveguide to a 1 μm multimode waveguide. Similarly, a taper of length 9 μm is used to couple the fundamental mode to a 1.8 μm multimode waveguide in the second-order mode converter. Performing the aforementioned calibration process, we get the ILs for both first- and second-order mode converters, as shown in Figs. 10(a) and 10(b), respectively. Specifically at 1550 nm, the ILs of the $TE_1$ and $TE_2$ modes are −2.0875 dB and −1.3745 dB for both fabricated first- and second-order mode converters, respectively. To reduce the error in the measurements due to fabrication error, the insertion loss to the higher-order mode is estimated by averaging the measured data of multiple fabricated devices.

In order to measure the crosstalks in our fabricated mode converters, we fabricate another system which contains only the mode converters without their inverse ones, as shown in Fig. 8(a). The fabricated systems for cross-talk measurements of both the $TE_0/TE_1$ and $TE_0/TE_2$ mode converters are located at the right and left of the figure, respectively. In this case the grating coupler detects only the crosstalk to the fundamental mode. The crosstalk to the higher-order modes cannot be measured as the grating coupler just detects the fundamental modes. As shown in Fig. 10, the measured crosstalks
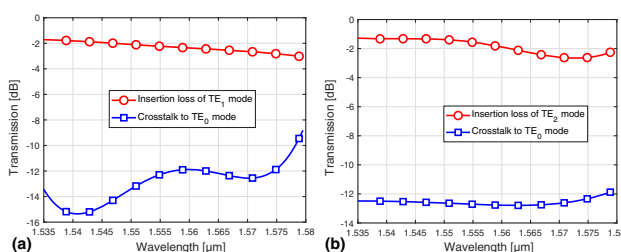
to the fundamental modes are −13.4055 dB and −12.6270 dB for both fabricated first- and second-order mode converters, respectively.

The results of ILs and CTs show good agreement between simulation and experimental data in the same wavelength range. The little differences can be attributed to some of the unavoidable manufacturing challenges, e.g., the surface of the SOI wafer is not flat and has thickness variations across the wafer. These fabrication variations lead also to variations in the feature size of the fabricated device. However, the used theoretical model still gives a good indication for the performance of the fabricated device.

## 6. CONCLUSION

A high-order waveguide mode converter based on small substrips of a dielectric material has been proposed for SOI platforms. The mode converter is formed internally in the propagation waveguide at any position, using very short substrips of different dielectric material with a length that ranges from 0.6 μm to 0.8 μm. A mathematical model of the device has been developed in order to determine the design parameters of the device. With the aid of the obtained design parameters, the performance of the device has been simulated, fabricated, and tested for conversion from fundamental to both first- and second-order modes. An insertion loss that ranges from 1.28 dB to 1.9 dB has been achieved for different modes using different dielectric materials. Fabrication results show good agreement between simulated data and experimental data for both first- and second-order mode converters.

## REFERENCES

1. V. R. Almeida, R. R. Panepucci, and M. Lipson, "Nanotaper for compact mode conversion," Opt. Lett. **28**, 1302–1304 (2003).
2. D. Dai, Y. Tang, and J. E. Bowers, "Mode conversion in tapered submicron silicon ridge optical waveguides," Opt. Express **20**, 13425–13439 (2012).
3. K. T. Ahmmed, H. P. Chan, and B. Li, "Broadband high-order mode pass filter based on mode conversion," Opt. Lett. **42**, 3686–3689 (2017).
4. Y. Xiong, R. B. Priti, and O. Liboiron-Ladouceur, "High-speed two-mode switch for mode-division multiplexing optical networks," Optica **4**, 1098–1102 (2017).
5. D. González-Andrade, J. G. Wangüemert-Pérez, A. V. Velasco, A. Ortega-Moñux, A. Herrero-Bermello, I. Molina-Fernández, R. Halir, and P. Cheben, "Ultra-broadband mode converter and multiplexer based on sub-wavelength structures," IEEE Photonics J. **10**, 1–10 (2018).
6. B. Stern, X. Zhu, C. P. Chen, L. D. Tzuang, J. Cardenas, K. Bergman, and M. Lipson, "On-chip mode-division multiplexing switch," Optica **2**, 530–535 (2015).
7. K. Chen, S. Wang, S. Chen, S. Wang, C. Zhang, D. Dai, and L. Liu, "Experimental demonstration of simultaneous mode and polarization-division multiplexing based on silicon densely packed waveguide array," Opt. Lett. **40**, 4655–4658 (2015).
8. C. P. Chen, J. B. Driscoll, R. R. Grote, B. Souhan, R. M. Osgood, and K. Bergman, "Mode and polarization multiplexing in a Si photonic chip at 40 Gb/s aggregate data bandwidth," IEEE Photonics Technol. Lett. **27**, 22–25 (2015).



**Fig. 10.**   Measured results for fabricated (a) first-order and (b) second-order mode converters.

9. H. M. H. Shalaby, "Bi-directional coupler as a mode-division multiplexer/demultiplexer," J. Lightwave Technol. **34**, 3633–3640 (2016).

10. O. M. Nawwar, H. M. H. Shalaby, and R. K. Pokharel, "Modeling, simulation, and fabrication of bi-directional mode-division multiplexing (BMDM) for silicon-on-insulator platform," Appl. Opt. **57**, 42–51 (2018).

11. H. M. H. Shalaby, "Bidirectional mode-division multiplexers with anti-reflection gratings," Appl. Opt. **57**, 476–484 (2018).

12. J. Wang, S. He, and D. Dai, "On-chip silicon 8-channel hybrid (de) multiplexer enabling simultaneous mode- and polarization-division-multiplexing," Laser Photonics Rev. **8**, L18–L22 (2014).

13. K. Igarashi, D. Souma, T. Tsuritani, and I. Morita, "Performance evaluation of selective mode conversion based on phase plates for a 10-mode fiber," Opt. Express **22**, 20881–20893 (2014).

14. K. Igarashi, D. Souma, K. Takeshima, and T. Tsuritani, "Selective mode multiplexer based on phase plates and Mach-Zehnder interferometer with image inversion function," Opt. Express **23**, 183–194 (2015).

15. C. Koebele, M. Salsi, L. Milord, R. Ryf, C. A. Bolle, P. Sillard, S. Bigo, and G. Charlet, "40km transmission of five mode division multiplexed data streams at 100gb/s with low MIMO-DSP complexity," in European Conference and Exposition on Optical Communications (Optical Society of America, 2011), pp. Th–13.

16. W. Mohammed, M. Pitchumani, A. Mehta, and E. G. Johnson, "Selective excitation of the lp11 mode in step index fiber using a phase mask," Opt. Eng. **45**, 074602 (2006).

17. Y.-S. Lee, K.-S. Lim, M. Islam, M.-H. Lai, and H. Ahmad, "Dynamic lp01-lp11 mode conversion by a tilted binary phase plate," J. Lightwave Technol. **35**, 3597–3603 (2016).

18. P. Simonen, A. Heinonen, M. Kuulusa, and J. Nurmi, "Comparison of bulk and SOI CMOS technologies in a DSP processor circuit implementation," in 13th International Conference on Microelectronics, 2001. ICM 2001 Proceedings (IEEE, 2001), pp. 107–110.

19. G. Chen, R. Zhang, and J. Sun, "On-chip optical mode conversion based on dynamic grating in photonic-phononic hybrid waveguide," Sci. Rep. **5**, 10346 (2015).

20. S. M. Israelsen and K. Rottwitt, "Broadband higher order mode conversion using chirped microbend long period gratings," Opt. Express **24**, 23969–23976 (2016).

21. Z. Lu, H. Yun, Y. Wang, Z. Chen, F. Zhang, N. A. Jaeger, and L. Chrostowski, "Broadband silicon photonic directional coupler using asymmetric-waveguide based phase control," Opt. Express **23**, 3795–3808 (2015).

22. J. Wang, Y. Xuan, M. Qi, H. Huang, Y. Li, M. Li, X. Chen, Z. Sheng, A. Wu, W. Li, X. Wang, S. Zou, and F. Gan, "Broadband and fabrication-tolerant on-chip scalable mode-division multiplexing based on mode-evolution counter-tapered couplers," Opt. Lett. **40**, 1956–1959 (2015).

23. D. Chen, X. Xiao, L. Wang, Y. Yu, W. Liu, and Q. Yang, "Low-loss and fabrication tolerant silicon mode-order converters based on novel compact tapers," Opt. Express **23**, 11152–11159 (2015).

24. D. Ohana, B. Desiatov, N. Mazurski, and U. Levy, "Dielectric metasurface as a platform for spatial mode conversion in nanoscale waveguides," Nano Lett. **16**, 7956–7961 (2016).

25. W. Ye, X. Yuan, Y. Gao, and J. Liu, "Design of broadband silicon-waveguide mode-order converter and polarization rotator with small footprints," Opt. Express **25**, 33176–33183 (2017).

26. H. Okayama, Y. Onawa, D. Shimura, H. Yaegashi, and H. Sasaki, "Silicon wire waveguide TE 0/TE 1 mode conversion Bragg grating with resonant cavity section," Opt. Express **25**, 16672–16680 (2017).

27. L. F. Frellsen, Y. Ding, O. Sigmund, and L. H. Frandsen, "Topology-optimized mode converter in a silicon-on-insulator photonic wire waveguide," in Conference on Lasers and Electro-Optics (CLEO 2016) (2016), pp. STh3E.4(1–2).

28. B. E. Abu-elmaaty, M. S. Sayed, H. M. H. Shalaby, R. K. Pokharel, and A. Srivastava, "Silicon-on-insulator fundamental to first-order dual polarization mode converter based on Si-Si3N4 phase plate waveguide," in Proceedings of the 20th International Conference on Transparent Optical Networks (ICTON 2018) (Bucharest, 2018), pp. Tu.C5.5(1–4).

29. M. Dumitrescu and M. Guina, "Effective index method for computation of the propagation constant and electromagnetic field distribution in z-uniform dielectric or semiconductor waveguides," in Fifth Conference on Optics (Bucharest, 1997), pp. 922–925.

30. H. Furuta, H. Noda, and A. Ihaya, "Novel optical waveguide for integrated optics," Appl. Opt. **13**, 322–326 (1974).

31. R. K. Varshney and A. Kumar, "A simple and accurate modal analysis of strip-loaded optical waveguides with various index profiles," J. Lightwave Technol. **6**, 601–606 (1988).

32. K. S. Chiang, "Analysis of the effective index method for the vector modes of rectangular core dielectric waveguides," IEEE Trans. Microwave Theory Tech. **44**, 692–700 (1996).

33. M. Qiua, "Effective index method for heterostructure-slab-waveguide-based two-dimensional photonic crystals," Appl. Phys. Lett. **81**, 1163–1165 (2002).

34. A. Yariv, "Coupled-mode theory for guided-wave optics," IEEE J. Quantum Electron. **9**, 919–933 (1973).

35. E. Peral and A. Yariv, "Supermodes of grating-coupled multimode waveguides and application to mode conversion between copropagating modes mediated by backward Bragg scattering," J. Lightwave Technol. **17**, 942–947 (1999).